Soil Dynamics and Earthquake Engineering 119 (2019) 130–143

Contents lists available at ScienceDirect

Soil Dynamics and Earthquake Engineering

journal homepage: www.elsevier.com/locate/soildyn

Seismic responses of an underground powerhouse structure subjected to oblique incidence SV and P waves

Xiaowei Wang[a,b], Juntao Chen[a,b,*], Ming Xiao[a,b]

[a] State Key Laboratory of Water Resources and Hydropower Engineering Science, Wuhan University, Wuhan 430072, China
[b] Key Laboratory of Rock Mechanics in Hydraulic Structural Engineering, Ministry of Education, Wuhan University, Wuhan, China

ARTICLE INFO

Keywords:
Underground powerhouse structure
Seismic responses
Viscous-spring artificial boundary
Oblique incidence seismic waves
Rock-structure interaction

ABSTRACT

In this work, the impacts of seismic motion incident angles and the rock-structure interaction (RSI) on the seismic response of an underground powerhouse structure of a hydropower station are studied. Based on the viscous-spring artificial boundary condition, the input methods of oblique incidence SV and P waves are presented by transforming the seismic motion into equivalent nodal forces acting on the nodes of artificial boundaries. Based on the explicit central difference method, an explicit dynamic contact analysis method considering the bonding and damage characteristics of the contact face between the surrounding rock and the underground powerhouse structure is also proposed. Consequently, the proposed methods are implemented into an dynamic finite element program and applied to the seismic damage evolution process analysis for the concrete structure of an underground powerhouse, and the results reveal that (1) the stress and deformation response of the underground powerhouse structure caused by seismic excitations are clearly affected by the incident angle and its degree of damages reaches a maximum when the incident angle is 30°; (2) compared to the case of without the RSI, the damage distribution ranges and the damage coefficient of the underground powerhouse structure are much larger than that in the case of with the RSI; and (3) the contact state of the contact face plays a key role in the dynamic stability of the underground powerhouse structure, and a good contact state can help to reduce the dynamic damage of the underground structure.

1. Introduction

Southwest China is rich in water resources, with a number of large hydropower stations located there. These hydropower underground powerhouses are generally composed of several long-span and high sidewall caverns that are located in areas of high seismic intensity, which will have a great impact on the overall safety of the hydropower stations if an earthquake disaster occurs. Numerous studies have been conducted to study the dynamic response of underground caverns [1–7], with many achievements having been obtained. However, the researches have mainly focused on the surrounding rock, while few studies have investigated the dynamic response of the underground structures. The "Wenchuan" earthquake disaster investigation [8,9] showed that the surrounding rock of an underground powerhouse in the earthquake area is generally stable, but the seismic damage to the underground structure is serious, which means that the underground structure is a weak component in the seismic design of an underground powerhouse, and its seismic response characteristics have a high theoretical and engineering significance.

The dynamic time history method is an effective method for analyzing the seismic response of complex large-scale structures. The seismic response time history analysis of an underground powerhouse structure mainly includes two aspects: one is the seismic motion input for the finite element model, and the other is the dynamic contact analysis of the surrounding rock and underground structure. It is well known that whether or not the input method of the seismic motion is reasonable will directly affect the accuracy and credibility of the calculation results. In the existing numerical calculations of underground structures, it is mostly assumed that the seismic motion is a vertical incidence from the bottom of the numerical model. In reality, when the epicenter is close to the engineering site of the underground structure, the seismic motion is usually obliquely incident [10]. According to the statistics data of strong earthquake observation records in recent years, it was determined that the incident angle of the seismic motion for a bedrock site is approximately 60° [11,12]. This oblique incidence seismic wave will produce spatial non-uniform effects on the underground structure. Some scholars are currently studying the influence of oblique incidence seismic motion on underground structures. Du et al.

* Corresponding author at: State Key Laboratory of Water Resources and Hydropower Engineering Science, Wuhan University, Wuhan 430072, China.
E-mail address: chenjt@whu.edu.cn (J. Chen).

https://doi.org/10.1016/j.soildyn.2019.01.014
Received 5 August 2017; Received in revised form 18 December 2018; Accepted 9 January 2019
0267-7261/ © 2019 Elsevier Ltd. All rights reserved.

[13] analyzed the seismic response rules of underground engineering under oblique incidence SV waves, and the results showed that the dynamic response of an underground structure in the case of oblique incidence seismic motion is clearly larger than that in the case of vertical incidence. Zhao et al. [14] studied the seismic response of large caverns under different incident directions of seismic motion, with the result showing that oblique incidence seismic motion has negative effects on the stability of rock caverns. Zhang et al. [15] developed the spatial oblique incidence method of seismic motion for the seismic response analysis of underground caverns, taking the spatial non-uniform effect of seismic motion into consideration. Heymsfield et al. [16] studied the effects of oblique incidence SH waves on the displacement of the free surface of an inclined bedrock. Naggar et al. [17] studied the impacts of seismic motion incident angles on the bending moment and thrust of composite tunnel lining. Huang et al. [18] studied the influences of incident angles of P waves on the seismic response of a long tunnel based on the time-history finite element method and viscoelastic artificial boundary condition. Stamos et al. [19] presented a new boundary element method to study the seismic response of long tunnels under oblique incidence body waves. It can be seen from the above that the current studies on oblique incidence seismic motion have made several achievements, but studies on the effects of 3D (three-dimensional) oblique incidence seismic motion on the seismic response of underground powerhouse structures have not yet been reported.

Because the seismic RSI is of complex nonlinear characteristics, an efficient seismic contact analysis model as well as its solving algorithm are required for large-scale nonlinear calculations. Currently, the dynamic contact problems of a complex contact system are mainly solved by numerical methods, such as the Lagrange multiplier method [20], the penalty function method [21], the contact element method [22] and the numerical programming method [23]. However, these methods spend a large amount of computation time and memory space, and sometimes the iteration does not converge. Therefore, they cannot be effectively applied to the dynamic contact analysis of large underground structures. The dynamic contact force method proposed by Liu et al. [24] combines the contact conditions with the explicit centre difference method. This method has been widely applied to the dynamic contact analysis of large complex engineering with a better convergence and no iteration [25], but the bonding effects of the contact face are not considered. In fact, due to the grouting effect, the lining structure in the underground powerhouse is strongly bonded to the surrounding rock before the contact face begins cracking. Thus, the cohesion of the contact face between lining structure and surrounding rock can not be ignored.

According to the above review, the input methods of 3D oblique incidence SV and P waves are established in Section 2 based on viscoelastic artificial boundary conditions as well as wave the field decomposition principle. Combined with the proposed explicit dynamic contact analysis method that considers the bonding and damage characteristics of the contact face between the lining structure and surrounding rock in Section 3, a dynamic response analysis method of an underground powerhouse structure under oblique incidence seismic waves is constructed. The analysis method is applied to the dynamic calculation of an underground powerhouse of a hydropower station, and the seismic damage evolution of the underground powerhouse structure is studied in Section 4. These results could provide references for anti-seismic designs of large underground powerhouse.

2. Input method of oblique incidence seismic waves

In the seismic response analysis of large underground structures via the finite element method, it is necessary to intercept the limited computing model from the infinite domain foundation and introduce appropriate artificial boundary conditions on the boundary of the model to simulate the radiation damping effect of an infinite domain foundation. The seismic load is a kind of external excitation, and the input method of seismic motion is closely related to the artificial boundary conditions. Therefore, it is necessary to deal with the artificial boundary problems before the seismic motion input.

According to seismic wave mechanics, the artificial boundary condition should ensure that the propagation characteristics of seismic waves at the artificial boundary are consistent with those in the original continuum, which means the scattering waves in the calculation model can enter the infinite domain through the artificial boundary without reflection. Numerous artificial boundary conditions have been proposed based on different computational theories [26–30], among which the viscoelastic artificial boundary is the most widely used because its physical meaning is simple and clear and it can describe the spatio-temporal decoupling in the process of solving the seismic wave problem. Based on the 3D viscoelastic artificial boundary conditions proposed by Du et al. [31], as well as the seismic wave field decomposition principle, an input method of 3D oblique incidence P waves for finite element simulation of an underground powerhouse structure is established in this section by transforming the seismic motion into equivalent nodal forces acting on the nodes of artificial boundaries.

2.1. 3D viscous-spring artificial boundary

The 3D viscoelastic artificial boundary is a stress-type time domain artificial boundary that achieves the absorption of the scattered seismic waves by setting the spring and damping system in the directions of the three freedoms of the boundary nodes, as shown in Fig. 1. According to the derivation of paper [31], the spring-damping parameters of the artificial boundary are

In the normal direction

$$K_N = \frac{1}{1+\alpha}\cdot\frac{\lambda + 2G}{r} \quad C_N = \beta\rho c_p \tag{1}$$

In the tangential direction

$$K_T = \frac{1}{1+\alpha}\cdot\frac{G}{r} \quad C_T = \beta\rho c_s \tag{2}$$

where K_N and C_N are the normal spring and damping parameters of the artificial boundary, respectively; K_T and C_T are the tangential spring and damping parameters of the artificial boundary, respectively; G, ρ and λ are the shear modulus, density and Lame constant of the infinite domain medium, respectively; r is the distance from the epicenter to the artificial boundary; C_P and C_S are the compression wave and shear wave velocities of the infinite domain medium, respectively; α represents the amplitude ratio of the plane wave to the scattered seismic waves, and β represents the relationship of the physical wave velocity and apparent wave velocity. In this paper, their values are advised to be 0.8 and 1.1 [31], respectively.

2.2. The solutions for a free wave field and equivalent loads on the artificial boundaries

After setting the artificial boundary, the accurate seismic motion input requires that the displacements and stresses on the artificial

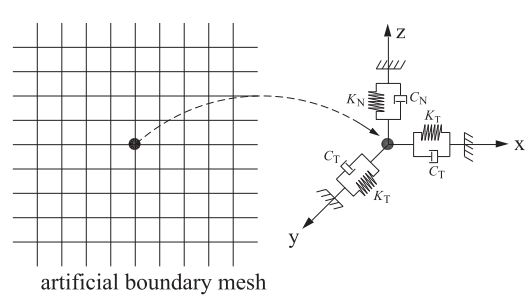

Fig. 1. Viscoelastic artificial boundary physical schematic.

boundary should be the same as the original free wave field. According to the seismic wave field decomposition theory, the displacement field u^T at the artificial boundary can be decomposed into a free field u^F formed by incident waves and a scattering field u^S caused by structural effects, namely: $u^T = u^F + u^S$.

The scattering seismic waves at the artificial boundary are absorbed by the spring-damping element and can be obtained by the finite element time integral in the calculation model, while the free wave field needs to be converted into nodal forces and acted upon the artificial boundary nodes. Liu et al. [32] achieved the input of seismic motion by converting it into an equivalent node force. The equivalent node force P_{li} at direction i of node l at the artificial boundary can be written as

$$P_{li} = (C_{li}\dot{u}_{li}^F + K_{li}u_{li}^F + \sigma_{li}^F)A_l \tag{3}$$

where σ_{li}^F is the stress of the free wave field in a continuous medium; C_{li} and K_{li} are the spring and damping coefficients in direction i of node l, and can be obtained according to Eqs. (1) and (2), respectively; u_{li}^F and $\dot{u}_{li}^F$ are the displacement and velocity of the free wave field, respectively; A_l is the equivalent area for the boundary node l. It can be seen from Eq. (3) that the key to solving the equivalent node force P_{li} lies on the solution of free field displacement u_{li}^F.

The factors that affect the free wave field at the artificial boundary mainly include two aspects: one is that the incident seismic waves will generate a wave transformation at the free surface of the half space, where the incident SV and P waves can be decomposed into reflected P and SV waves, respectively. Then, the incident wave field at the artificial boundary becomes the superposition of the wave field generated by the incident SV or P wave, reflected P wave and reflected SV wave, as shown in Fig. 2. The other factor is that the input of the seismic motion into the calculation model of a large underground powerhouse structure is usually from multiple artificial boundaries. The distances of the nodes on these artificial boundaries with the epicenter are different, so the arrival times of the incident seismic wave to the nodes are different, and the seismic wave received by the nodes at the same time must also have a phase difference. To consider the impacts of the above two factors on the free wave field, two basic assumptions need to be introduced: (1) the free surface at the top of the calculation model is horizontal; and (2) the infinite domain medium is a uniform elastic medium, regardless of the attenuation of the seismic wave propagation process. Thus, the general expression for the displacement u_{li}^F can be written as

At the lateral artificial boundary

$$u_{li}^F = u_{SV_1}^F + u_{SV_2}^F + u_{P_2}^F \quad \text{for incident SV waves} \tag{4}$$

$$u_{li}^F = u_{P_1}^F + u_{P_2}^F + u_{SV_2}^F \quad \text{for incident P waves} \tag{5}$$

At the bottom artificial boundary

$$u_{li}^F = u_{SV_1}^F \quad \text{for incident SV waves} \tag{6}$$

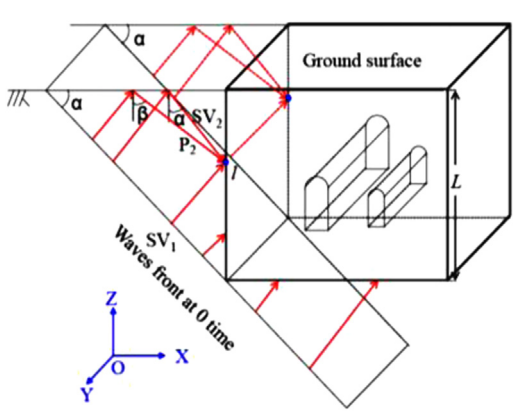

Fig. 2. Diagram of oblique incidence of plane SV waves.

$$u_{li}^F = u_{P_1}^F \quad \text{for incident P waves} \tag{7}$$

where $u_{SV_1}^F/u_{P_1}^F$, $u_{SV_2}^F$ and $u_{P_2}^F$ are the displacements generated by the input SV or P waves, and reflected SV and P waves, respectively.

Assuming the incident wave front is parallel to the axis of the underground powerhouse, and $u_0(t)$ is the displacement of the input plane SV or P waves, then according to the geometrical relationship between the artificial boundary node l and the incident wave front, the expressions of $u_{SV_1}^F$, $u_{SV_2}^F$ and $u_{P_1}^F$, $u_{P_2}^F$ at node l can be obtained:

$$\begin{aligned} u_{SV_1}^F &= u_0(t-\Delta t_1)[\cos\alpha, 0, -\sin\alpha]^T \\ u_{SV_2}^F &= B_1u_0(t-\Delta t_2)[-\cos\alpha, 0, -\sin\alpha]^T \quad \text{for incident SV waves} \\ u_{P_2}^F &= B_2u_0(t-\Delta t_3)[\sin\beta_1, 0, -\cos\beta_1]^T \end{aligned} \tag{8}$$

$$\begin{aligned} u_{P_1}^F &= u_0(t-\Delta t_3)[\sin\alpha, 0, \cos\alpha]^T \\ u_{P_2}^F &= B_3u_0(t-\Delta t_4)[-\sin\alpha, 0, \cos\alpha]^T \quad \text{for incident P waves} \\ u_{SV_2}^F &= B_4u_0(t-\Delta t_5)[\cos\beta_2, 0, \sin\beta_2]^T \end{aligned} \tag{9}$$

where α is the incident angle between the incident wave front and the free surface; β_1 and β_2 are the reflection angles of the incident waves at the free surface and $\beta_1 = \arcsin(c_P\sin\alpha/c_S)$, $\beta_2 = \arcsin(c_s\sin\alpha/c_p)$; c_s and c_p are the wave speeds of the SV and P waves, respectively; B_1, B_2, B_3 and B_4 are the amplitude amplification factors of the reflected SV and P waves, and their values can be determined according to the seismic wave reflection law of the elastic half space surface; and Δt is time interval of the incident wave from the wave front to node $l(x_l, y_l, z_l)$, which is

$$\begin{aligned} \Delta t_1 &= |x_l\sin\alpha + z_l\cos\alpha|/c_S \\ \Delta t_2 &= |x_l\sin\alpha + (2L - z_l)\cos\alpha|/c_S \\ \Delta t_3 &= |x_l\sin\alpha + L\cos\alpha - (L - z_l)\tan\beta_1\sin\alpha|/c_S + |(L - z_l)/\cos\beta_1|/c_P \\ \Delta t_4 &= |x_l\sin\alpha + z_l\cos\alpha|/c_p \\ \Delta t_5 &= |x_l\sin\alpha + (2L - z_l)\cos\alpha|/c_p \\ \Delta t_6 &= |x_l\sin\alpha + L\cos\alpha - (L - z_l)\tan\beta_2\sin\alpha|/c_p + |(L - z_l)/\cos\beta_2|/c_s \end{aligned} \tag{10}$$

Obviously, the displacement u_{li}^F at the artificial boundary can be calculated according to Eqs. (4)–(10). It must be pointed out that the analytical expression is obtained under the assumption that the incident wave front is parallel to the axis of the underground powerhouse, and the calculations of the two examples in the sections below are both based on this assumption. If the incident wave front is not parallel to the principal direction of the calculation model, paper [18] offers a detailed analytical expression. The velocity $\dot{u}_{li}^F$ can be obtained from the derivative of displacement u_{li}^F to time, and the stress σ_{li}^F can be obtained according to the generalized Hooke's law. Then, the equivalent load P_{li} can be obtained by substituting u_{li}^F, $\dot{u}_{li}^F$ and σ_{li}^F into Eq. (3).

2.3. Numerical verification of the input method

To verify the accuracy and reliability of the input method, two numerical models are established to simulate the propagation process of a seismic wave in the semi-infinite elastic medium. The size of the finite element model for example 1 is 1200 × 1200 × 1200 m (as shown in Fig. 3). The model consists of 64000 elements, and the maximum mesh size is 50 m, which meets the mesh size requirement in the process of the seismic wave simulation. The elastic modulus, Poisson's ratio and density of the medium are 10 GPa, 0.3 and 3000 kg/m^3, respectively. The viscoelastic artificial boundaries are applied at the bottom of and around the model, while the top of the model is a free surface. The centre point (600,600,600) of the free surface is selected as the monitoring point. Fig. 4 is the displacement time history of the input P waves, whose peak displacement is 1.0 m.

Fig. 5(a) and (b) are the displacement time history curves of the monitoring point under 15° input angles of SV and P waves, respectively. The corresponding normal vectors of the wave front are (0.259,

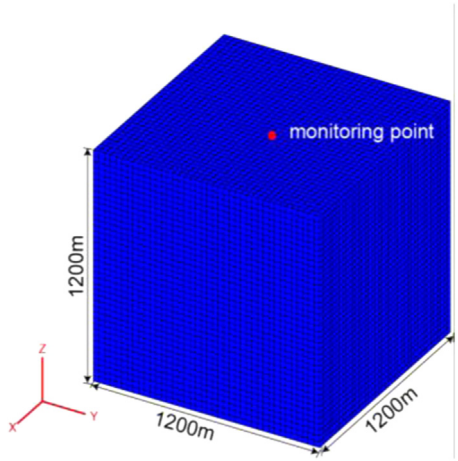

Fig. 3. 3D Finite element model for example 1.

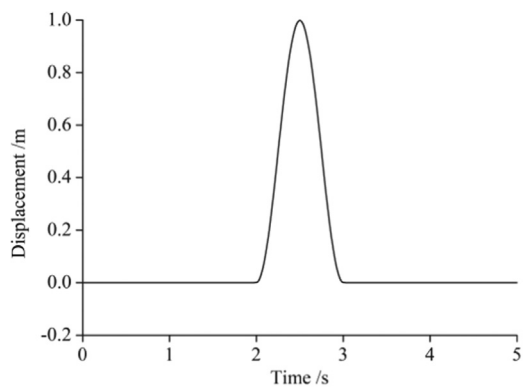

Fig. 4. Displacement time history of the incidence waves.

0, 0.966). It can be seen from Fig. 5 that the displacements of the X and Z directions of the monitoring point are in good agreement with the theoretical values.

Example 2 simulates the scattering of vertically incident seismic waves via a circular tunnel in elastic half-space. The model for the finite element calculation and its size are shown as Fig. 6. The tunnel is embedded at a depth of 1.5 m and its radius a is 2 m. The finite element calculation parameter of the medium in half space, i.e., the elastic modulus, Poisson's ratio and density, are 9 GPa, 0.3456, and 2750 kg/m^3, respectively. The displacement function of the incident wave is $u = \cos(851.3t)$ with amplitudes of $\boldsymbol{A}_0 = 1\boldsymbol{m}$ (shown in Fig. 7). As seen from Fig. 8 and Fig. 9, the normalized horizontal and vertical displacement amplitudes ($\boldsymbol{U}_x$ and $\boldsymbol{U}_z$) at the ground surface for the SV and

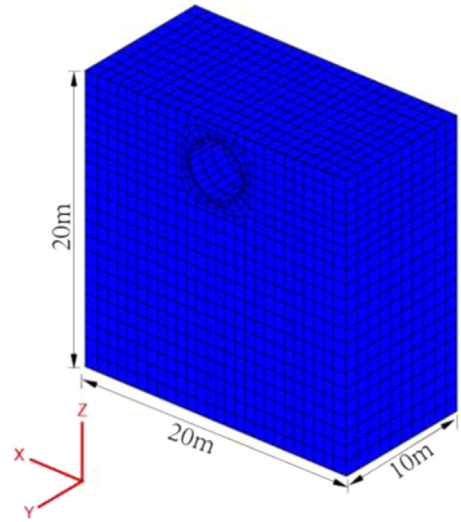

Fig. 6. 3D Finite element model for Example 2.

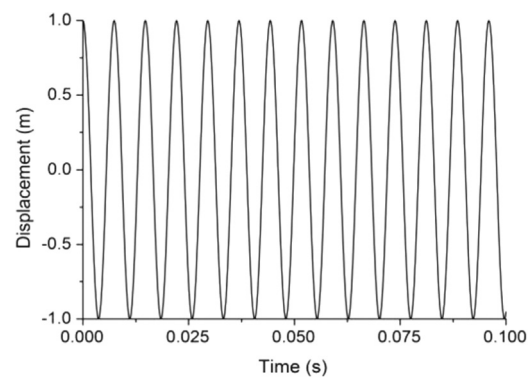

Fig. 7. Displacement time history of the incidence waves.

P waves calculated by the present method are compared with the results offered by Luco and De Barros and show good agreement, which means that the proposed input method can effectively simulate the seismic wave field of a semi-infinite elastic medium.

3. Dynamic contact analysis model of an underground powerhouse structure and the surrounding rock

The contact system consists of a large-scale underground structure, and the surrounding rock consists of complex contact states and numerous contact elements. Due to the grouting effect, the contact face

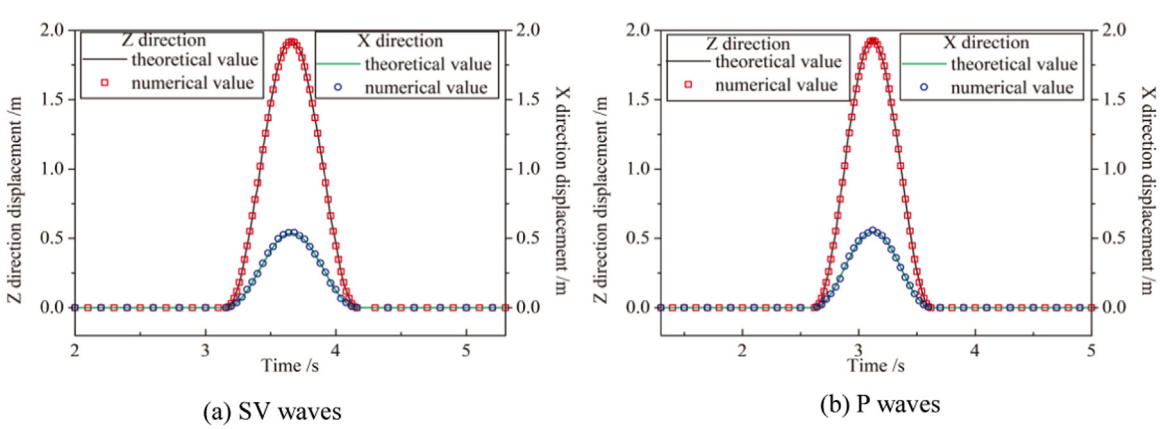

Fig. 5. Displacement time history of the monitoring point under 15° incident angles.

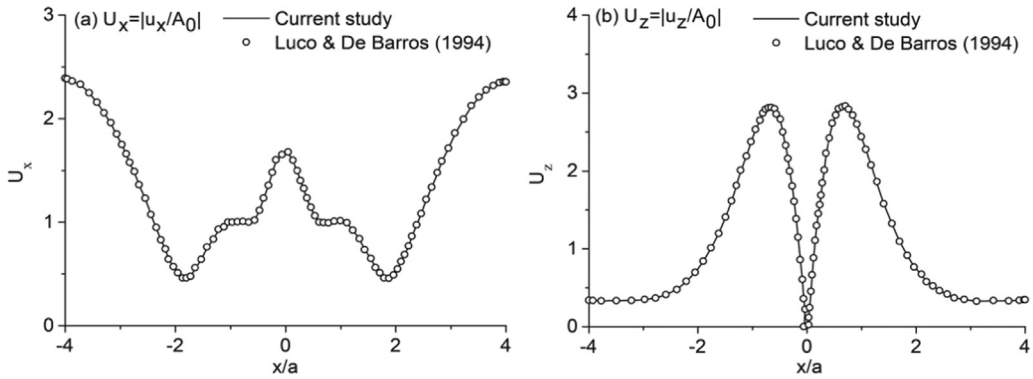

Fig. 8. Amplitudes of the total displacements along the free surface under vertical input SV waves: (a) horizontal component; (b) vertical component.

between the underground structure and surrounding rock is strongly bonded together with a certain shear strength and tensile strength before the bonding failure. Therefore, a reasonable dynamic contact model for an underground structure should not only be able to meet a large-scale nonlinear calculation but also describe the complex dynamic contact features. Based on the explicit time-domain integration method, a dynamic contact model for an underground structure, considering the contact conditions and bond behaviour of the contact face, is proposed in this section.

3.1. The explicit time-domain integration method for the motion equations of the contact system

Fig. 10 shows the contact system of the surrounding rock and the underground structure as well as the dynamic contact forces on the contact face. According to the idea of Liu [33],the contact face S can be divided into two sides of surface S_1 for the surrounding rock and S_2 for the underground structure. The correspondent nodes on surface S_1 and S_2, such as i and i' in Fig. 10, are namely, node pairs (pairs of nodes). The two nodes of each node pair own identical local coordinate systems and global coordinates, and the node forces of the two nodes meet the interaction relationship of $N_i + N_{i'} = 0$ and $T_i + T_{i'} = 0$. This section mainly derives the time-domain integration scheme for the node displacements of the contact system according to the motion equations.

After finite element discretization, the dynamic equilibrium equation of the nodes on the contact face under a seismic action can be written as

$$M\ddot{U} + C\dot{U} + KU = N + T + F \tag{11}$$

where N and T are the normal and tangential contact force vectors, respectively. F is the known external force vector. $\ddot{U}$, $\dot{U}$ and U represent the acceleration vectors, velocity vectors and displacement vectors, respectively. M, C and K represent the mass matrix, damping matrix and stiffness matrix. The mass matrix is expressed by a lumped mass

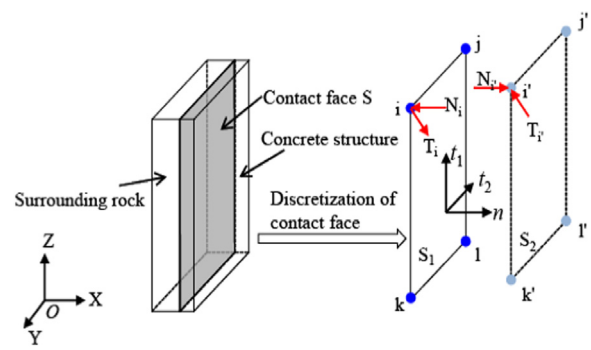

Fig. 10. Contact model and dynamic contact force on the contact face.

matrix and the damping matrix adopts the Rayleigh damping matrix

$$M = \int \rho[\phi]^T[\phi]dv \tag{12}$$

$$C = \omega M + \xi K \tag{13}$$

where $[\phi]$ is the matrix for function ϕ_i, whose value is 1 or 0. ω and ξ are damping constants.

Solving the motion equation according to central difference method, the explicit integral expressions of the motion equations at time $n + 1$ can be written as

$$U^{n+1} = \overline{U}^{n+1} + \Delta t^2 M^{-1}(N^n + T^n)/2 \tag{14}$$

$$\dot{U}^{n+1} = 2(U^{n+1} - U^n)/\Delta t - \dot{U}^n \tag{15}$$

$$\ddot{U}^{n+1} = 2(\dot{U}^{n+1} - \dot{U}^n)/\Delta t - \ddot{U}^n \tag{16}$$

$$\overline{U}^{n+1} = U^n + \Delta t\dot{U}^n + \Delta t^2 M^{-1}(F^n - KU^n - C\dot{U}^n)/2 \tag{17}$$

Where Δt represents the time step.

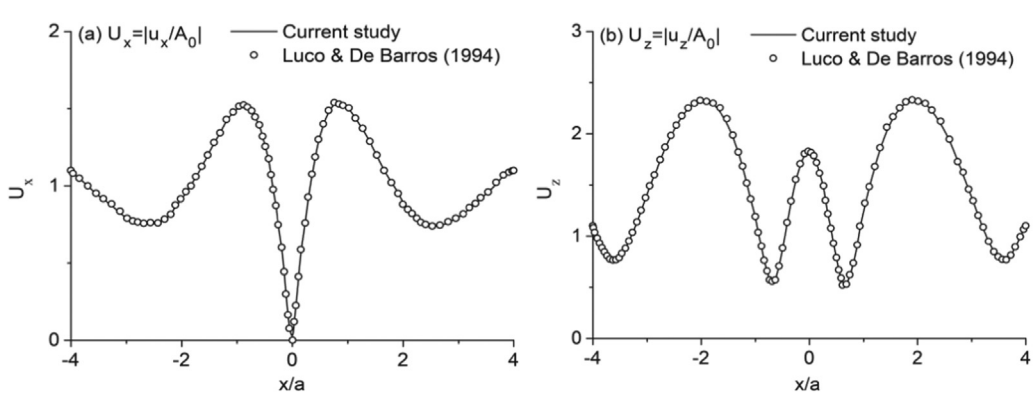

Fig. 9. Amplitudes of the total displacements along the free surface under vertically input P waves: (a) horizontal component; (b) vertical component.

Obviously, it can be seen from Eqs. (14)–(17) that the motion states at time $n+1$ can be obtained by the displacements, velocities and contact forces of the nodes at time n. However, N^n and T^n are two unknowns and depend on the motion state at time $n+1$ as well as at time n. Thus, it is essential to first calculate the contact force N^n and T^n based on the contact conditions.

3.2. Contact conditions and the solution of the dynamic contact force

The key of the dynamic contact calculation is to solve the dynamic contact forces of the nodes on the contact face. The core idea of the solution is to first predict and then modify. Namely: it is first assumed that the node pairs are in a bonding state so we can obtain the contact forces by the displacement constraint conditions of the nodes on the contact face, then we can correct the calculated contact force according to the force constraint conditions.

It is assumed that the surrounding rock and the underground structure are in a bonding state, and the node pair satisfies the constraint condition with no relative displacement in the normal and tangential directions:

$$H_i(U_{i'}^{n+1}-U_i^{n+1}) = \begin{Bmatrix} U_{i'1}^{n+1} - U_{i1}^{n+1} \\ U_{i'2}^{n+1} - U_{i2}^{n+1} \\ U_{i'3}^{n+1} - U_{i3}^{n+1} \end{Bmatrix} = \begin{Bmatrix} U_{i'1}^{n} - U_{i1}^{n} \\ U_{i'2}^{n} - U_{i2}^{n} \\ 0 \end{Bmatrix} \tag{18}$$

where U_i^{n+1} and $U_{i'}^{n+1}$ are the displacement vectors of nodes i and i', respectively, Eq. (18) also applies to other node pairs on the contact face. The subscripts 1, 2, and 3 of U represent the tangential (t_1, t_2) and normal (n) components of the nodal displacements along the contact face (as shown in Fig. 6). H_i represents the transformation matrix for the global and local coordinate system of the contact node i, that is,

$$H_i = \begin{pmatrix} t_{1i} \\ t_{2i} \\ n_i \end{pmatrix} = \begin{bmatrix} t_{1i,1} & t_{1i,2} & t_{1i,3} \\ t_{2i,1} & t_{2i,1} & t_{2i,1} \\ n_{i1} & n_{i2} & n_{i3} \end{bmatrix} \tag{19}$$

Substituting Eq. (14) into Eq. (18),

$$\begin{pmatrix} T_{1i}^n \\ T_{2i}^n \\ N_i^n \end{pmatrix} = \frac{2M_iM_{i'}}{(M_i+M_{i'})\Delta t^2} \begin{bmatrix} \bar{U}_{i'1}^{n+1} - \bar{U}_{i1}^{n+1} - (U_{i'1}^n - U_{i1}^n) \\ \bar{U}_{i'2}^{n+1} - \bar{U}_{i2}^{n+1} - (U_{i'2}^n - U_{i2}^n) \\ \bar{U}_{i'3}^{n+1} - \bar{U}_{i3}^{n+1} \end{bmatrix} \tag{20}$$

where T_{1i}^n and T_{2i}^n are sub-vectors of the tangential force along directions t_1 and t_2, respectively. Therefore,

$$T_i^n = T_{1i}^n + T_{2i}^n \tag{21}$$

Obviously, the contact forces in Eqs. (20) and (21) are achieved on the assumption that the contact face is in a bonding state. However, the contact face is the weak part of the underground structure, and its damage under the seismic cyclic loads is difficult to avoid. In fact, there are several contact states between the surrounding rock and the underground structure under the seismic cyclic load, such as the bonding contact, sliding contact and separation. Therefore, it is essential to check and correct the contact forces on the contact face.

The most common damage forms of the contact face are shear slip in the tangential direction and tensile cracking in the normal direction. This paper recalibrates the contact state and corrects the contact forces from the following aspects.

(1) If $N_i^n \cdot n_i > 0$ and $\|N_i^n\| > \sigma_t A_i$, then the contact forces are in a tension state, and tensile cracks occur on the contact face. Then, the contact forces should be corrected as

$$N_i^n = 0, \ \ T_i^n = 0 \tag{22}$$

(2) If $N_i^n \cdot n_i > 0$ and $\|N_i^n\| \le \sigma_t A_i$, then the contact forces are in a tension state, but the tensile stress is smaller than the tensile strength of the contact face. Then, it only needs to correct the tangential contact force as follows

$$T_i^n = 0 \tag{23}$$

(3) If $N_i^n \cdot n_i \le 0$, then the contact face is in a contact state, and only the tangential contact force needs to be calibrated. Namely, if $\|T_i^n\| > \mu_s \|N_i^n\| + cA_i$, it means that shear slip occurred on the contact face. Thus, the tangential contact force should be corrected as

$$T_i^n = \mu_d \|N_i^n\| \frac{T_i^n}{\|T_i^n\|} \tag{24}$$

where c and σ_t represent the initial cohesion and tensile strength of the contact face, respectively. A_i is the control area by node i. μ_s and μ_d are the static friction coefficient and kinetic friction coefficient, respectively. Note that if there is any tensile crack or shear slip on the contact face, the cohesion correction of $c = 0$ is required. The contact forces N^n and T^n can be achieved by Eqs. (20)–(24). Then, substituting them into Eqs. (14)–(17), the motion state of the contact nodes at time $n+1$ can be updated.

4. Numerical application

4.1. Problem layout

The underground powerhouse structures of a hydropower station have the characteristics of a large size, complex structure, etc. Because of the mutual restraint and interaction between the structure and the surrounding rock, the response characteristics of the underground structure under an earthquake load are complicated. For this study, the input method of 3D oblique incidence P waves is established in Section 2, and the dynamic contact analysis model of the surrounding rock and underground structure is established in Section 3. Both of them are implemented in this section into an in-house dynamic FEM numerical simulation platform [34] by a self-developed Fortran program and employed to investigate the impacts of the incident angles of seismic motion and the RSI on the seismic response of an underground powerhouse structure.

4.2. 3D FEM model and calculation conditions

Fig. 11 shows the FEM model of an underground powerhouse. The model mainly consists of a main powerhouse and main transformer cavern (as shown in Fig. 12), and their sizes are 13.7 × 21.0 × 39.4 m and 13.7 × 17.1 × 26.9 m (length × width × height), respectively. The analysis model consists of 142,745 nodes and 134,232 hexahedron elements (eight nodes), 7378 of which are concrete structure elements. The maximum mesh size is 5 m and meets the requirement of the dynamic calculation accuracy. To study the stress and displacement response of the concrete structure, the middle section of the model is selected as the typical section, of which six monitoring points on the structures of the main powerhouse and main transformer cavern are taken as the research objects. The specific arrangements are shown in Fig. 13.

The buried depth of the underground powerhouse is approximately 150 m. The surrounding rock is class III_1, and the underground powerhouse structure is made of C25 concrete. The concrete thicknesses of the roof arches, sidewalls and floors are 1 m, 0.8 m and 0.5–1 m, respectively. The surrounding rock adopted the elastoplastic damage constitutive model based on Mohr-coulomb criterion [34], while the concrete structures adopted a plastic damage constitutive model. The scalar damage factor D for concrete can be expressed as [35]

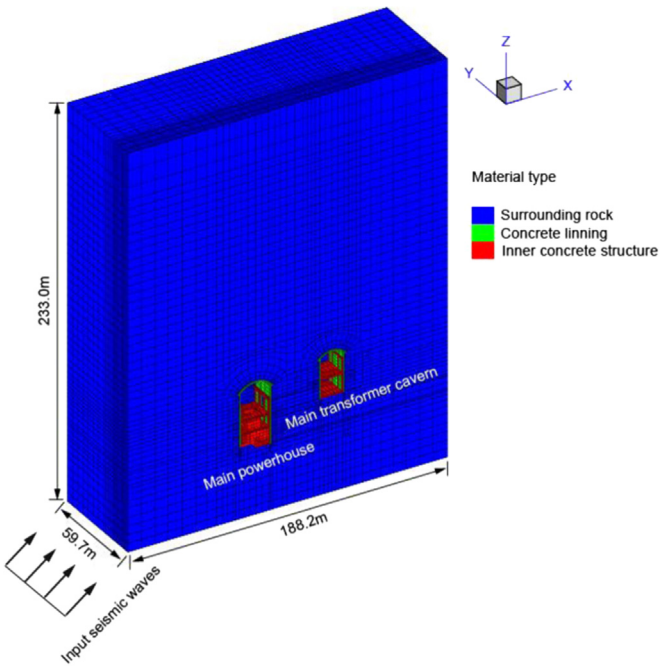

Fig. 11. Part of the 3D finite element model.

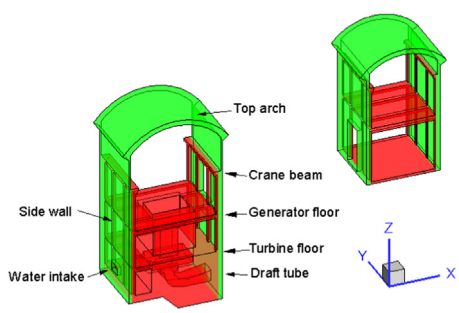

Fig. 12. Schematic diagram of underground powerhouse structure.

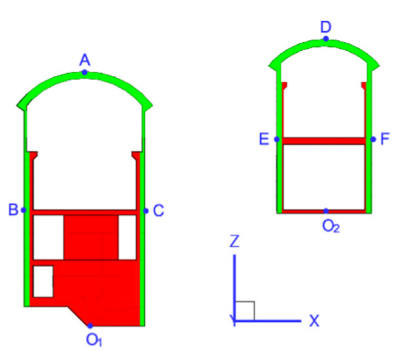

Fig. 13. Layout of the monitoring points.

$$D = 1 - (1 - d_c)(1 - sd_t)$$
$$d_t = 1 - \frac{(1 - A_t)\varepsilon_t^f}{\bar{\varepsilon}^p} - \frac{A_t}{\exp[B_t(\bar{\varepsilon}^p - \varepsilon_t^f)]}$$
$$d_c = 1 - \frac{(1 - A_c)\varepsilon_c^f}{\bar{\varepsilon}^p} - \frac{A_c}{\exp[B_c(\bar{\varepsilon}^p - \varepsilon_c^f)]} \tag{25}$$

where s is the stiffness restitution coefficient when the state of tension is transferred to a compression state. d_t and d_c are the tensile and compression damage coefficients, respectively. A_t, B_t and A_c, B_c are the tensile and shear damage parameters and can be fitted according to the experimental results. $\bar{\varepsilon}^p$ is the equivalent plastic strain. ε_t^f and ε_c^f are the thresholds for the tensile and shear damage, respectively. The physical mechanical parameters of the materials used in the calculation are shown in Table 1.

Table 1
Mechanical parameters of the model materials.

Materials	Rock mass	Concrete	Contact surface
Elastic modulus(GPa)	9.0	25	
Density(kg/m^3)	2750	2500	
Poisson's ratio	0.27	0.17	
Friction angle(°)	42	47.7	40
Cohesion c(MPa)	1.05	1.3	1.0
Tensile yield stress (MPa)	1.3	1.27	1.0
Compressive yield stress (MPa)	35	16.7	

The simulation process is divided into two steps: static excavation and dynamic calculation. In the first step, the gravity field is adopted as an initial stress field due to the lack of measured geostress data, and the stress state computed in this step is used as the initial condition for the dynamic calculation. In this process, the effects of the supports, i.e., lining and rockbolts, are determined by the method of Chen et al. [36]. The mechanical behaviours of the rockbolts are modelled by the implicit cylindrical anchor bar element [37], and the reinforcing effect of the rockbolts on the surrounding rock is realized by superimposing the stiffness of the anchor bar element into that of the anchored rock. In the next step, the viscoelastic artificial boundaries around and at the bottom of the model, are used to absorb the energy of the scattered seismic wave field, while the top is a free surface. Since an explicit integration method is adopted to solve the seismic wave field in the simulation platform, an appropriate time step Δt is required to meet the accuracy of the solution [38]

$$\Delta t \le \alpha \min_e \frac{l_e}{C_e} \quad (0.80 \le \alpha \le 0.98) \tag{26}$$

where α is an empirical coefficient; C_e is the wave velocity; and l_e is the minimum size of the element.

The acceleration time history of the 1940 El Centro earthquake (North-south, and peak acceleration = 3.49 m/s^2) is adopted in this paper. The first 20 s of the acceleration time history are intercepted and the peak acceleration is adjusted to 1.7 m/s^2 according to China's existing regulations. This is then input into the finite element model by the method described in Section 2 with different input angles of 0°, 15°, 25°, and 30° for the SV waves and 0°, 30°, 60°, and 90° for the P waves. The input acceleration time history is shown in Fig. 14. Note that there is a critical incident angle $\alpha_0 = \arcsin(c_s/c_p) = 34°$ for the SV waves, and the case where the incident angle of the SV waves is over the critical angle α_0 is not considered in this paper.

4.3. Impacts of the incident angles of seismic motion on seismic response of the underground structure

The fact that an oblique incidence seismic wave has negative effects on the stability of an underground structure is widely recognized. However, there are few studies on the specific impacts of the incident angles on the complex underground powerhouse structure of a hydropower station. In this section, the impacts of the input angles on the seismic response of an underground powerhouse structure are analyzed from three aspects: stress, displacement and damage state.

4.3.1. Oblique incidence SV waves

4.3.1.1. Stress response of the underground structure. The tensile strength of concrete is much smaller than its compressive strength, so tension failure is a common damage form for concrete material. The maximum principle stress time history of point A (at the top arch of the main powerhouse) is selected for analysis (as shown in Fig. 15). It can be determined that the maximum principal stresses are approximately

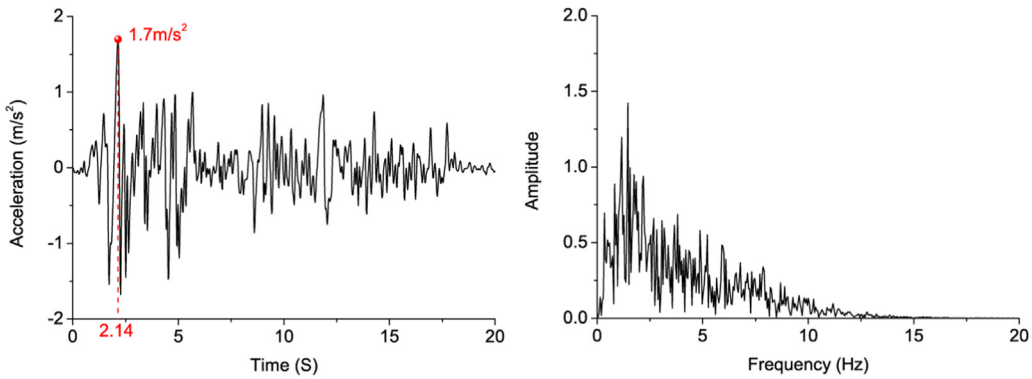

Fig. 14. Time-history (left) and Fourier spectrum (right) of the input acceleration.

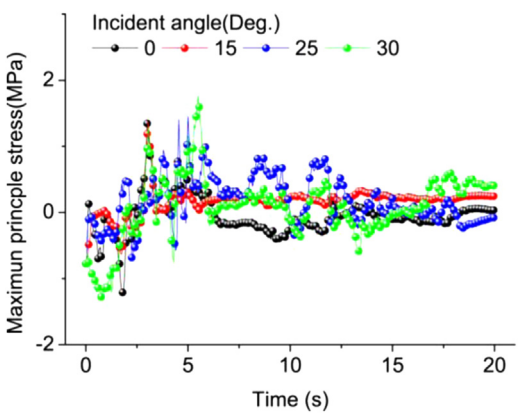

Fig. 15. Maximum principle stress time-history curve of point A.

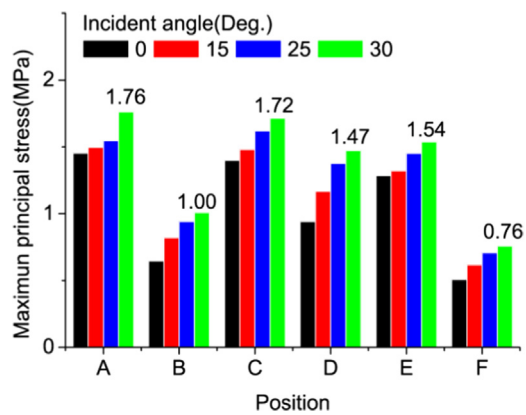

Fig. 16. Peak value of maximum principle stress.

−0.78 MPa at time 0 s, and the fluctuation amplitudes of their time history curves are small in the period of 0–2.5 s. From 2.5 to 10 s the curves fluctuate violently, with their fluctuation ranging from −0.7 to 1.76 MPa. Their peak values under different incident angles are almost all higher than the concrete tensile strength (1.2 MPa). In the period of 10–20 s, the fluctuation amplitudes begin to decrease, and the maximum principal stresses are finally stabilized in the range of −0.08 to 0.41 MPa. Compared with Fig. 14 and Fig. 15, it is obvious that the maximum principal stress time history curves are similar to that of the input seismic wave, which indicates the fluctuation laws of the stress time history curves are mainly affected by the input seismic wave. Moreover, the stress responses are significantly different for the same position under different seismic wave input angles. As the incident angle increases, the fluctuations of the maximum principal stress are more intense, and the fluctuation ranges are much larger when the incident angles are 25° and 30°.

The effects of the seismic waves input angles on the peak values of the maximum principal stresses are demonstrated in Fig. 16. It can be seen that the peak values of the maximum principal stress increase when the input angles increase, reaching a maximum value when the incident angle is 30°, which means the seismic wave field condition of the underground structure is complex and there is more reflection magnification at the subsurface of the structure under oblique incidence seismic motion, which contributes to larger additional dynamic stresses. The stress distributions have obvious differences at different positions of the underground structure; the peaks of the maximum principal stress of the roof arches (point A and D) are larger than that of the sidewalls (points B, C, E, and F). Furthermore, the left sidewall (point B) has a larger stress response than that of right sidewall (point C) at the main powerhouse, while the opposite is true for the main transformer cavern.

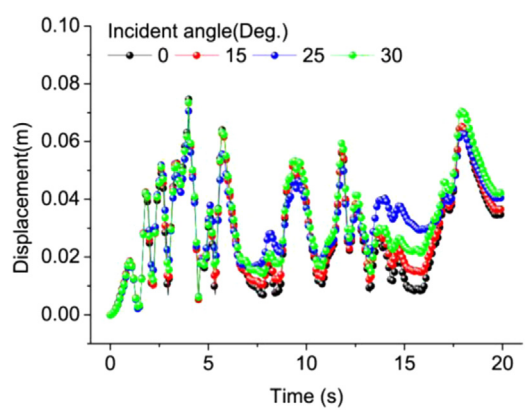

Fig. 17. Displacement time history curve of point A.

4.3.1.2. Displacement response of underground structure. Fig. 17 offers displacement time history curves of the roof arch (point A) of the main powerhouse under different incident angles. Because the displacement fluctuation laws of other positions are similar to that of point A, they are not individually listed in this paper. It can be concluded that the waveforms and fluctuation laws of the 4 time history curves are quite similar to one another, and the peaks and valleys appear almost simultaneously, indicating that the incident angles of the ground motion have little effect on the displacement fluctuation law of the underground structure. The main difference of the curves lies in the fluctuation amplitudes, which increase with an increase of the incident angle and reach a maximum of 0.074 m under a 30° incident angle. The underground structure may have an overall deformation under seismic action, so a relative displacement is introduced to analyse the structural deformation. In this paper, the relative displacement peak is defined as

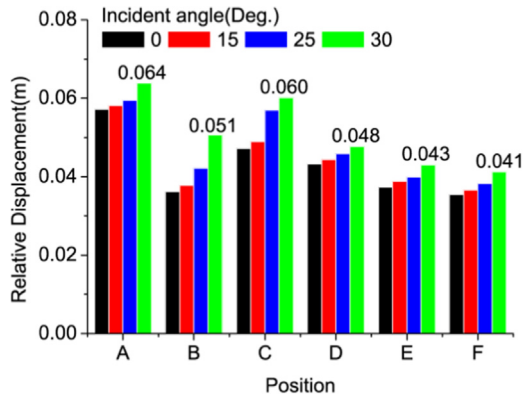

Fig. 18. Peak value of relative displacement.

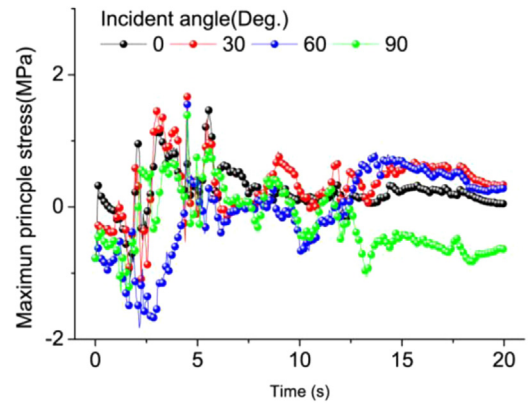

Fig. 20. Maximum principle stress time-history curve of point A.

the displacement peak of monitoring points (A, B, C and D, E, F) with the corresponding centre point (O_1 and O_2) of the floor on the typical section, which is plotted in Fig. 18. From Fig. 18, it can be observed that the relative displacements of the six monitoring points increase with an increase in the incident angle. The deformation of the underground structure is the largest when the incident angle is 30°. The deformation of the roof arch is slightly larger than that of the sidewalls, while the structure deformation of the main powerhouse is larger than that of the main transformer cavern. Therefore, it can be stated that the incident angle of the seismic motion has a greater impact on the displacement response of the large-scale structure.

4.3.1.3. Damage coefficient of the underground structure. The damage coefficient of the underground structure can directly reflect its seismic damage degree. The impacts of the incident angles of the SV waves on the damage coefficient distribution of the underground structure are plotted in Fig. 19. It is clear that the damage zone is mainly distributed in the roof arch and the internal concrete structure, such as the generator floor, the turbine floor and the generator windshield when the incident angle is 0° (as shown in Fig. 19(a)). The damage coefficient for the majority of the area is approximately 0.3, while the maximum damage coefficient does not exceed 0.5. With the increase in the incident angle, the damage area began to expand to the sidewalls of the main powerhouse and the roof arch of the main transformer cavern. The damage coefficient of the generator floor and other local areas have increased, the maximum of which is approximately 0.6 (as shown in Fig. 19(b) and Fig. 19(c)). When the incident angle is 30° (as shown in Fig. 19(d)), the overall damage degree of the underground structure reaches a maximum. Most areas of the main powerhouse are covered by the damage zone, while the damage zone of the roof arch and the upstream sidewall of main transformer cavern tend to connect. Therefore, it can be concluded that the overall damage degree of the underground structure increases with an increase of the incident angle.

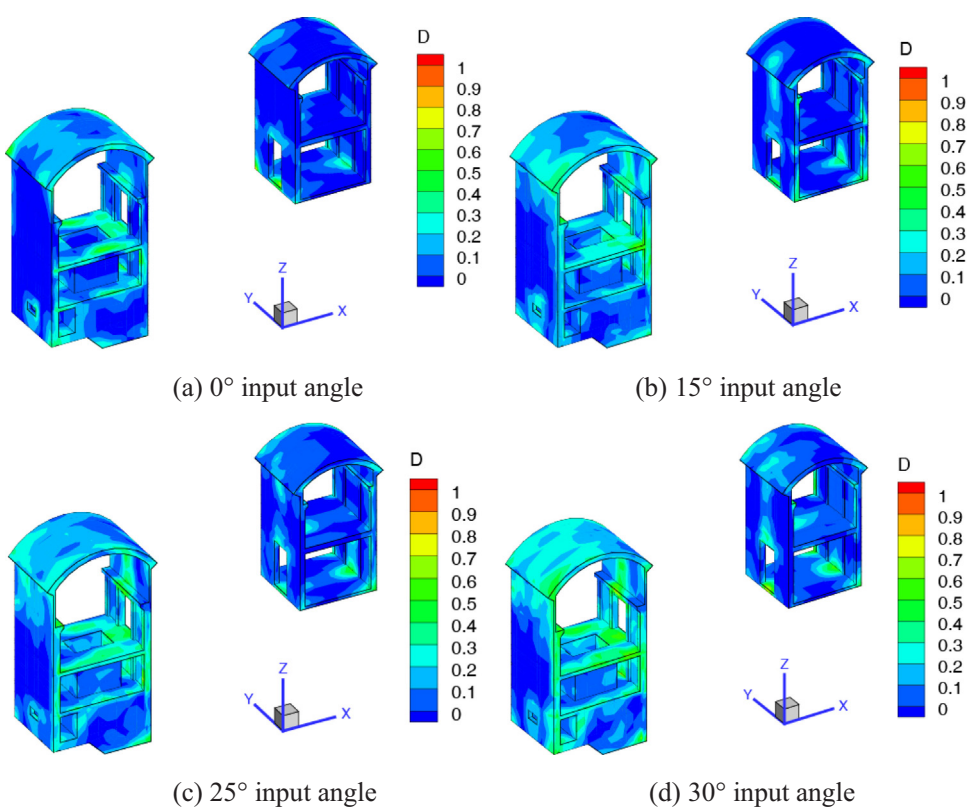

Fig. 19. Damage coefficient distribution of underground structure under different input angles of SV waves.

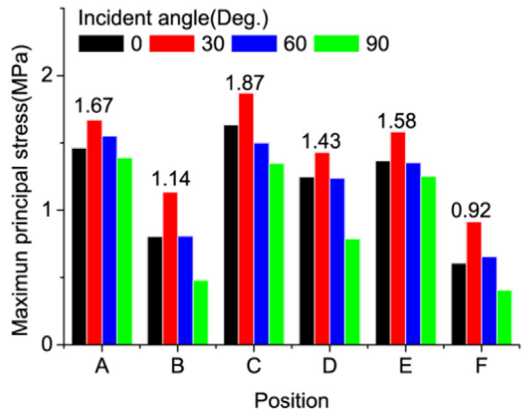

Fig. 21. The peak value of maximum principle stress.

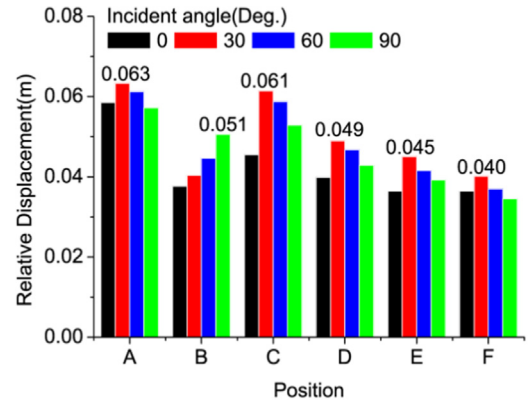

Fig. 23. Peak value of the relative displacement.

4.3.2. Oblique incidence P waves

4.3.2.1. Stress response of the underground structure. The maximum principle stress time history curves of the top arch (point A) of the main powerhouse subjected to oblique incidence P waves is shown in Fig. 20. Obviously, the fluctuation laws of the curves are similar to that of the curves in Fig. 15. The curves fluctuate violently with a wide fluctuation range of −1.69 to 1.67 MPa in the period of 2.5–10 s and their peak values are completely above the concrete tensile strength (1.2 MPa) under different incident angles, which means the underground structure has experienced a strong stress response and tensile damage has occurred during this period. Moreover, the stress responses of the structure to different input angles of seismic motion are clearly different. Compared with the vertical or horizontal incident waves, the 30° and 60° incident angles contribute to more intense stress fluctuations.

Fig. 21 shows the peak values of the maximum principal stresses at different positions of the main powerhouse and main transformer cavern with different input angles. According to Fig. 21, the peak values of the maximum principal stress first increase and then decrease with an increase in the incident angles and have a maximum incident angle under 30°, which means that the non-uniformity of the seismic motion caused by the oblique incidence seismic waves leads to a larger additional dynamic stress than the horizontal and vertical incident waves. Therefore, we can conclude the incident angle play an important role on the stress response of underground structure, and it is essential to consider the impacts of the incident angles on the seismic response of a large underground structure in anti-seismic design.

4.3.2.2. Displacement response of the underground structure. Fig. 22 displays the displacement time history curves of the roof arch (point A) of the main powerhouse subjected to different incident angles. As shown in Fig. 22, the waveforms of the curves are roughly similar, while their peaks and valleys appear nearly at the same time. The major difference of the curves is their fluctuation amplitudes, which increase with an increasing incident angle and reach a maximum of 0.084 m when the incident angle is 90°. However, it does not necessarily mean that the deformation of the underground structure is larger when the incident angle is 90° [13]. The overall deformation of the underground structure may occur under seismic action, so the relative displacement is more representative. As show in Fig. 23, the relative displacements of the six points first increase and then decrease with an increase in the incident angle, and the deformation of the underground structure reaches a maximum when the incident angle is 30°.

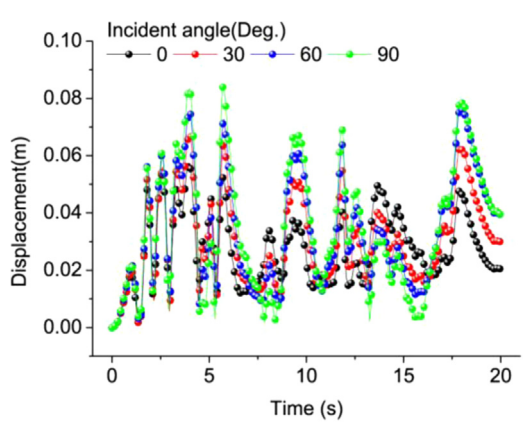

Fig. 22. Displacement time history curve of point A.

4.3.2.3. Damage coefficient of the underground structure. The damage coefficient distributions of the underground structure under P waves are depicted in Fig. 24(a)-(d). As seen, when the incident angle is 0°, the damage zone of the main powerhouse is mainly distributed in the roof arch and the internal concrete structure with a damage coefficient of approximately 0.3 in most of the damage area. With an increase in the incident angle, the damage areas begin to expand to the sidewalls of the main powerhouse and the roof arch of the main transformer cavern. The overall damage degree of underground structure reaches a maximum under a 30° incident angle, while the damage zones occupy most areas of the main powerhouse and tend to expand further at the roof arch and sidewall of main transformer cavern. As the incident angles continue to increase, the damage area begins to shrink, and the damage coefficient begins to decrease in some areas. The overall degree of damage of the underground structure is minimal when the incident angle is 90°, with the damage area mainly distributed in the roof arch and generator floor of the structures.

4.4. Impacts of the RSI on the seismic response of the underground structure

For the underground structure in a rock mass, the seismic response is mainly controlled by the extrusion and constraint effects of the surrounding rocks. Therefore, research of the RSI can contribute to analyzing the seismic response of the underground structure more rationally. In this section, the dynamic contact model (with the RSI) presented in Section 3 and the equivalent continuous model (without the RSI) are used to compare and analyse the impacts of the RSI on the seismic response of an underground structure subjected to SV waves and P waves. According to the results in Section 4.3, it can be observed that the underground structure has a maximum seismic response when the incident angle is 30°, so a 30° incident angle is adopted in the above two calculation models in this section.

4.4.1. Damage coefficient and damage type distribution of the underground structure

To study the effects of the RSI on the dynamic response of an

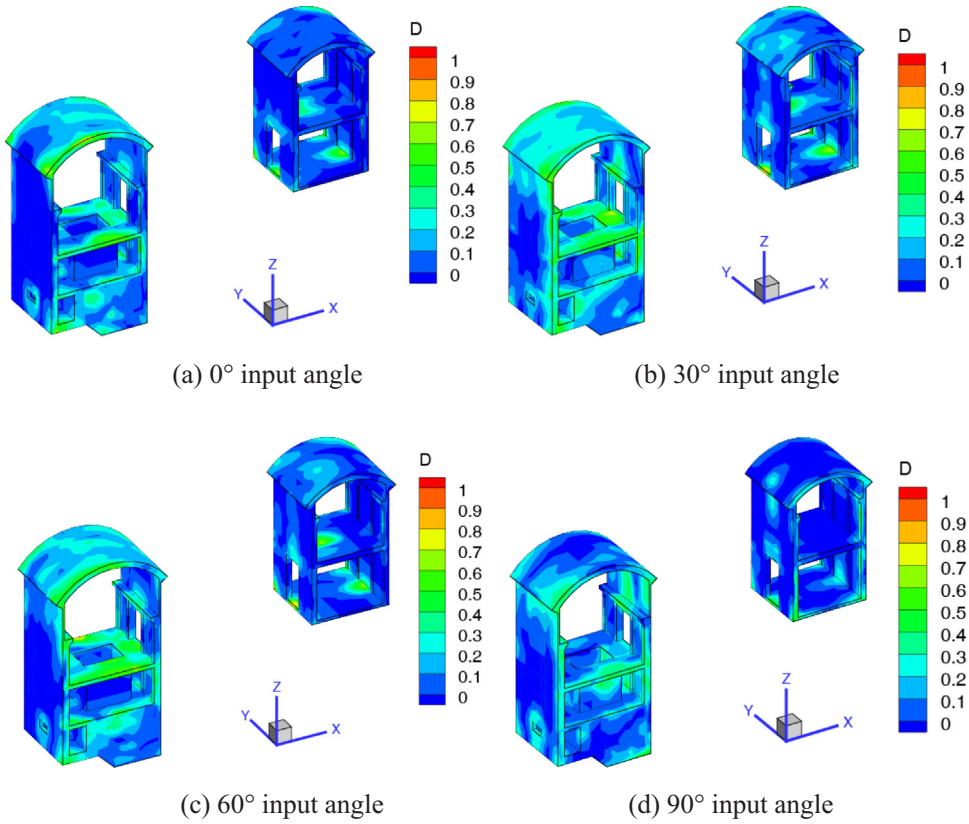

(a) 0° input angle (b) 30° input angle

(c) 60° input angle (d) 90° input angle

Fig. 24. Damage coefficient distribution of the underground structure under different input angles of P waves.

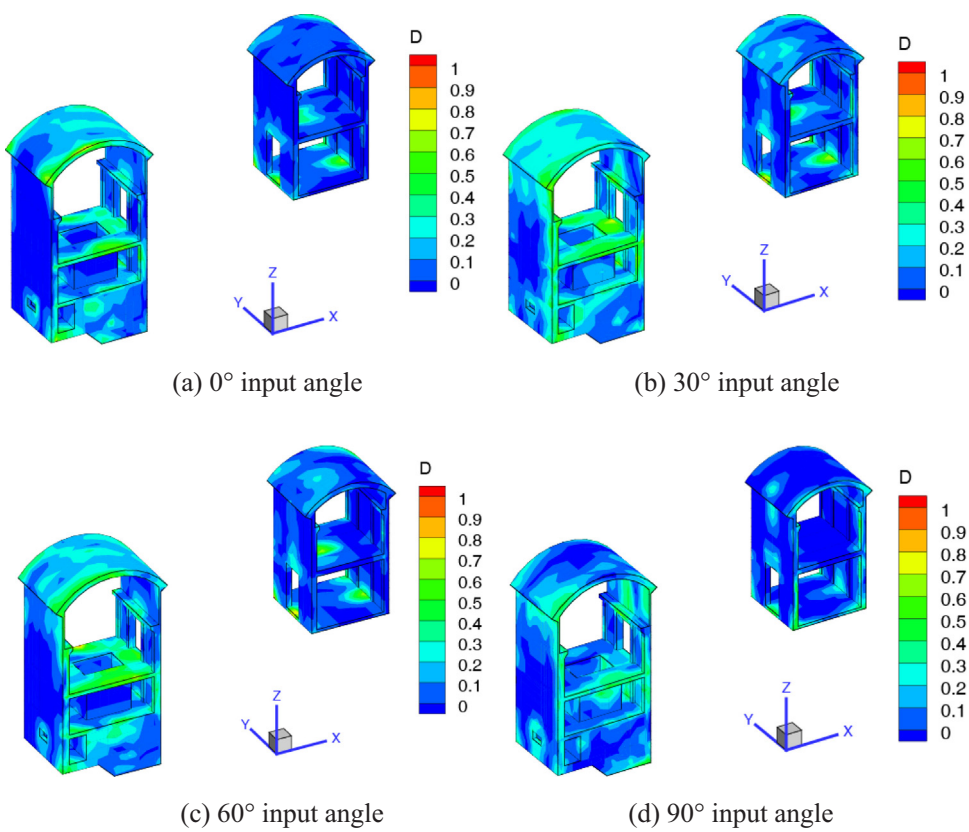

(a) 0° input angle (b) 30° input angle

(c) 60° input angle (d) 90° input angle

Fig. 25. Damage coefficient distribution without an RSI.

underground structure, the damage coefficient distribution of the underground structure with and without RSI under a 30° incident angle of SV waves are depicted in Fig. 19(d) and Fig. 25(a), respectively, while in Fig. 24(b) and Fig. 25 (b) for P waves, respectively. It is obvious that the damaged areas of the roof arches and sidewalls are larger, and the damage coefficient of the floors is slightly larger in the case of the RSI as shown in Fig. 19(d) and Fig. 24(b). It is mainly because the surrounding rock and the underground structure are a whole system in the case of without the RSI, and there is no relative displacement between the two. For the non-linear deformation considered in the case of including the RSI, the restraint effect of the surrounding rock on the underground structure is weaker and leads to a greater seismic response.

The damage types of the underground structure are mainly tensile and shear damage under the seismic actions of SV waves and P waves. As shown in Fig. 25, tensile damage is mainly distributed in the roof arches and floors of the underground structure, while shear damage occurs in the roof arches and sidewalls in the cases of with and without the RSI. The cracking area of the roof arches and the floors and the shear damage area of the sidewalls are clearly wider in the case of with the RSI than that of without the RSI, which means that the RSI has obvious effects on the damage distribution of the underground structure. Moreover, taking Fig. 19(d), Fig. 24(b), Fig. 25 and Fig. 26 into account, it can be concluded that the damage coefficient of the tensile damage zone is relatively large, and the damage situation is relatively serious, so crack control measures are necessary for the anti-seismic design of underground structures.

4.4.2. Damage distribution of the contact face of the surrounding rock and underground structure

The RSI mainly relies on the contact surface of the surrounding rock and the lining structure to transmit the load and displacement, so the contact state of the contact surface has a great influence on the seismic response of the underground structure. The lining structure is adhered to the surrounding rock. If considering the surrounding rock as a whole, it is obvious that the integrity of the lining and surrounding rock is not as strong as that of the rock mass itself. Therefore, it is difficult for the surrounding rock and lining structure to deform in synchrony under seismic cyclic actions, giving rise to slipping and cracking on their contact face, which is shown in Fig. 27. According to the distribution of slip and cracks on the contact face, the damage areas are mainly at the roof arches and the upper sidewalls. This is mainly due to the large free surface of the roof arches and the upper sidewalls, which leads to an easier slip and cracking for the contact surface. Moreover, combined with Fig. 26 and Fig. 27, it is obvious that there is an accordance of distribution between the slip and crack areas of the contact face and the structure damage areas. This means that a good contact state of the lining and surrounding rock is significant to the stability of the lining structure, and the constraint effect of the surrounding rock on the lining structure can efficiently reduce the seismic damage of the lining structure.

5. Summary and conclusions

Based on the 3D viscoelastic artificial boundary conditions, a 3D oblique input method of plane SV and P waves for an underground structure is established. Its accuracy and reliability are verified using two 3D numerical examples. Combined with the proposed explicit dynamic contact model considering bonding and damage characteristics of the contact face between the lining and surrounding rock, a dynamic response analysis method of the underground powerhouse structure under an oblique incidence of seismic motion is constructed. The method is applied to analyse the seismic damage evolution process of a concrete structure of an underground powerhouse. The impacts of the incident angles and the RSI on the seismic response of an underground powerhouse structure is studied, and the major conclusions can be drawn as follows:

(1) The impact of the incident angles of the seismic motion on the stress response of the underground structure mainly lies in the amplitudes of the stress fluctuation. In the case of input SV waves, the stress fluctuation peaks increase with an increase in the incident angles, while the stress fluctuation peaks first increase and then decrease with the propagating angles of the input P waves reaching a maximum at a 30° incident angle.
(2) The deformation response of the underground structure is obviously affected by the incident angles, and it reaches a maximum at a 30° incident angle of the SV and P waves. Moreover, the non-uniformity of the seismic motion caused by oblique incidence seismic waves

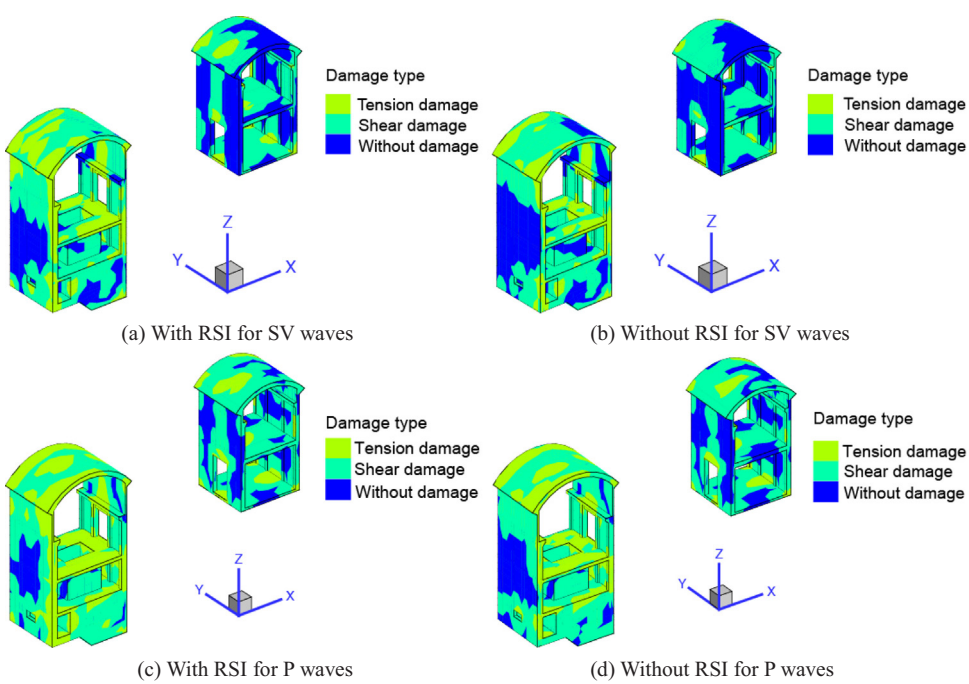

Fig. 26. Tension and shear damage distribution of the underground structure.

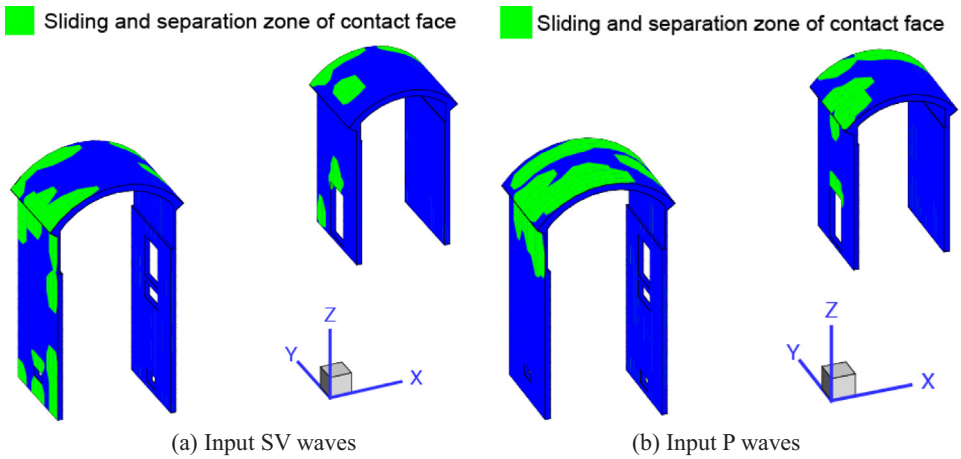

Fig. 27. Sliding and separation zone distribution of the contact face under SV waves and P waves.

leads to a spatial difference of the structure deformation and a greater deformation response than that of vertical or horizontal incidence seismic motion.

(3) The plastic damage of the underground powerhouse structure is sensitive to the incident angles of the SV and P waves, and it reaches the most serious damage under a 30° incident angle in the two cases, which is coincident with the stress and deformation response. The weak parts of the underground powerhouse structure under seismic actions are places that have a large free surface, such as the roof arches and the floors. Compared to vertical or horizontal incidences, these places suffer more serious damage under oblique incidence seismic waves.

(4) In the case of the RSI, the damage zone and damage coefficient of the underground structure are slightly larger than that without the RSI under oblique incidence SV and P waves. Additionally, the damage type of the regions with a larger damage coefficient is mainly tension damage, indicating that the anti-crack design is essential for anti-seismic design of underground structures.

(5) The contact state of the contact face between the surrounding rock and underground structure plays a key role in the stability of the underground structure, and the constraint effect of the surrounding rock on the underground structure is favourable for the underground structure stability under seismic action.

Acknowledgements

This study is supported by the National Key Basic Research Program of China (973 program) (Grant no. 2015CB057904), the Major Program of the National Natural Science Foundation of China (Grant nos. 51579191 and 51279136). The supports are greatly acknowledged and appreciated.

Conflict of interests

The authors declare that there is no conflict of interests regarding the publication of this paper.

References

[1] Aydan Ö, Ohta Y, Geniş M, et al. Response and stability of underground structures in rock mass during earthquakes. Rock Mech Rock Eng 2010;43(6):857–75.
[2] Hashash YMA, Hook JJ, Schmidt B, et al. Seismic design and analysis of underground structures. Tunn Undergr Space Technol 2001;16(4):247–93.
[3] Cui Z, Sheng Q, Leng X. Control effect of a large geological discontinuity on the seismic response and stability of underground rock caverns: a case study of the Baihetan# 1 surge chamber. Rock Mech Rock Eng 2016;49(6):2099–114.
[4] Li HB, Zhu L, Lv T. Seismic response analysis of an underground cavern groups in rock subjected to spatially non-uniform seismic ground motion. Chin J Rock Mech Eng 2008;27(9):1758–66.
[5] Chern JC, Chang YL, Lee HC. Seismic safety analysis of Kukuan underground power cavern. Tunn Undergr Space Technol 2004;19:4–5.
[6] Chen JY, Hu ZQ, Lin G. Random seismic response analysis of large-scale underground caverns. J Hydraul Eng 2002;1:71–5.
[7] Xu Y, Dai F. Dynamic response and failure mechanism of brittle rocks under combined compression-shear loading experiments. Rock Mech Rock Eng 2018;51(3):747–64.
[8] Yuting Zhang, Ming Xiao, Yujie Li. Effect of Wenchuan earthquake on earthquake damage and dynamic response analysis of underground powerhouse of Yingxiuwan hydropower station. Chinese. J Rock Mech Eng 2010;29(S2):3663–71.
[9] Zhiguo Zhang. Study on numerial simulation methods for seismic response of underground cavern complexs [Ph.D.thesis]. Wuhan: Wuhan University; 2012.
[10] Du Xiuli CW, Liang L, Liyun L. Preliminary study of time-domain seismic response for underground structures to obliquely incident seismic waves. Technol Earthq Disaster Prev 2007;2(3):290–6.
[11] Xing JN, Liao ZP. Statistical research on S-wave incident angle. Earthq Res China 1994;1:124–34.
[12] Sigaki Takahiro. Estimation of earthquake motion incident angle at rock site. In: Proceedings of the 12th world conference earthquake engineering. New Zealand: 2000. p. 956.
[13] Du XL, Huang JQ, Zhao M, et al. Effect of oblique incidence of SV waves on seismic response of portal sections of rock tunnels. Chin J Geotech Eng 2014;36(8):1400–6.
[14] Zhao B, Ma Z, Ding X. Seismic response of a large underground rock cavern groups considering different incident angles of earthquake waves. Chin J Rock Mech Eng 2010;29:3395–402.
[15] Zhang Z, Xiao M, Zhang Y, et al. Dynamic finite element analysis of large-scale complex underground caverns with three-dimensional elastoplastic damage model. Chin J Rock Mech Eng 2010.
[16] Heymsfield E. Two-dimensional scattering of SH waves in a soil layer underlain with a sloping bedrock. Soil Dyn Earthq Eng 2000;19(7):489–500.
[17] Naggar HE, Hinchberger SD, Naggar MHE. Simplified analysis of seismic in-plane stresses in composite and jointed tunnel linings. Soil Dyn Earthq Eng 2008;28(12):1063–77.
[18] Huang JQ, Du XL, Jin L, et al. Impact of incident angles of P waves on the dynamic responses of long lined tunnels. Earthq Eng Struct Dyn 2016;45(15):2435–54.
[19] Stamos AA, Beskos DE. 3-D seismic response analysis of long lined tunnels in half-space. Soil Dyn Earthq Eng 1996;15(2):111–8.
[20] Bathe KJ, Chaudhary A. A solution method for planar and axisymmetric contact problems. Int J Numer Methods Eng 1985;21(1):65–88.
[21] Perić D, Owen DRJ. Computational model for 3-D contact problems with friction based on the penalty method. Int J Numer Methods Eng 1992;35(6):1289–309.
[22] Belytschko T, Liu WK, Moran B, et al. Nonlinear finite elements for continua and structures[M]. John wiley & sons; 2013.
[23] Tangaramvong S, Tin-Loi F. An FE-MPEC approach for limit load evaluation in the presence of contact and displacement constraints. Int J Solids Struct 2012;49(13):1753–63.
[24] Liu J, Sharan SK. Analysis of dynamic contact of cracks in viscoelastic media. Comput Methods Appl Mech Eng 1995;121(1–4):187–200.
[25] Boyan Z, Houqun C. A new LDDA iterative algorithm for dynamic contact forces. Eng Mech 2007;24(6):1–6.
[26] Wolf JP, Song C. Finite-element modelling of unbounded modia. John Wiley; 1996. (326-326).
[27] Junyi Y, Feng J, Yanjie X, et al. A seismic free field input model for FE-SBFE coupling in time domain. Earthq Eng Eng Vib 2003;2(1):51–8.
[28] Deeks AJ, Randolph MF. Axisymmetric time -domain transmitting boundaries. J Eng Mech 1994;120(1):25–42.
[29] Liu J, Du Y, Du X, et al. 3D viscous-spring artificial boundary in time domain. Earthq Eng Eng Vib 2006;5(1):93–102.
[30] Kellezi L. Local transmitting boundaries for transient elastic analysis. Soil Dyn Earthq Eng 2000;19(7):533–47.
[31] Du X, Zhao M, Wang J. Stress artificial boundary in FEA for near-field wave

problem. Chin J Theor Appl Mech 2006;38(1):49–56.
[32] Liu J, Gu Y, Li B, et al. An efficient method for the dynamic interaction of open structure-foundation systems. Front Archit Civil Eng China 2007;1(3):340–5.
[33] Liu S, Liu J, Sun J, et al. A method for analyzing three-dimensional dynamic contact problems in visco-elastic media with kinetic and static friction. Comput Struct 2003;81(24–25):2383–94.
[34] Zhang ZG, Xiao M, Chen JT. Simulation of earthquake disaster process of large-scale underground caverns using three-dimensional dynamic finite element method. Chin J Rock Mech Eng 2011;30(3):510–23.
[35] Mazars J. A description of micro-and macroscale damage of concrete structures. Eng Fract Mech 1986;25(5):729–37.
[36] Chen J, Yang Y, Ye C, et al. Three-dimensional numerical analysis of compound lining in complex underground surge-shaft structure. Math Probl Eng 2015;2015.
[37] Xiao M. Analysis of 3D elasto-plastic finite element for underground implicit bolt element cave. Chin J Geotech Eng 1992;14(5):19–26.
[38] Liao ZP. Introduction to wave motion theories in engineering. Science 2002.